Synergistic role of poling in enhancing structural heterogeneity in perovskite piezoelectrics

Arnab De and Rajeev Ranjan*
Department of Materials Engineering, Indian Institute of Science, Bangalore-560012, India

(Received 20 May 2018; revised manuscript received 19 August 2018; published 24 September 2018)

Local structural heterogeneity is known to enhance the piezoelectric response of perovskite-based ferroelectrics. Here we investigate how this heterogeneity is affected by strong electric fields using dilute doped Eu^{+3} ions as local structural probes. We make use of the extreme sensitivity of the $^5D_0 \rightarrow {}^7F_2$ hypersensitive transition of Eu^{+3} vis-à-vis the asymmetric distribution of the ligand field around the doped ion to demonstrate that a strong electric field (poling) increases the overall low-symmetry regions on the local length scale in a $BaTiO_3$-based lead-free piezoceramic near the $P4mm$-$Amm2$ polymorphic phase boundary (PPB). Our study suggests that the mandatory treatment of poling given to a ceramic to make it piezoactive also contributes to the microscopic mechanisms that improve the system's piezo-response.

DOI: 10.1103/PhysRevB.98.094111

I. INTRODUCTION

The compactness, energy efficiency, and large impact force makes piezoceramics the preferred choice as pressor sensors, actuators, ultrasound motors, and transducers in wide-ranging applications. While the $Pb(Zr, Ti)O_3$ (PZT)-based piezoelectrics have been in use for more than five decades now, new directives [1,2] have oriented the scientific community to look for a suitable replacement of Pb-based piezoelectrics. The discovery of extraordinary piezoelectric response in $BaTiO_3$-based piezoelectric is one of the major achievements [3]. In addition to its great technological importance, this material system also provides an opportunity for a better understanding of the microscopic mechanisms that contribute to large piezoelectricity in ferroelectrics. $BaTiO_3$-based piezoelectrics differ qualitatively from the conventional piezoelectrics, such as PZT, in the following two ways: (i) the occurrence of high piezoelectric response in $BaTiO_3$ occurs at the tetragonal ($P4mm$)– orthorhombic ($Amm2$) phase boundary (instead of the $P4mm$-$R3m$ boundary in PZT), and (ii) the proximity of this boundary to a region in the phase diagram where four phases (the three ferroelectric phases and the cubic ($Pm3m$) paraelectric) converge [4]. Although concepts like polarization rotation/phase transformation [5,6], enhanced contribution of domain walls [7–9], and domain engineering [10,11] have generally been invoked to explain the increase of piezoelectricity in $BaTiO_3$-based piezoelectrics, recent detailed investigations have also revealed the important role of large fluctuations of the polarization in the orthorhombic phase because of the combined effect of a flat free-energy landscape and a fragmented local structure [12], confirming that structural heterogeneity is an important factor contributing to piezoelectricity enhancement in this system. This scenario is often associated with the piezoelectric ceramics in the unpoled state. Real piezoceramics must be mandatorily subjected to a strong electric field (traditionally known as poling treatment) to make it piezo-active. In view of the importance of local structural heterogeneity vis-à-vis the piezoelectric performance of piezoceramics [13,14], a relevant question is: *Does the poling affect the overall heterogeneity of the system?* From a structural perspective a heterogeneity can be treated as a low-symmetry local distortion as compared to the average symmetry perceived on the global scale by techniques such as x-ray/neutron diffraction. In piezoceramics, the electric field moves the ferroelectric-ferroelastic domain walls and/or interphase boundaries (in case of polymorphic/morphotropic phase boundary systems). The local low-symmetry distortions can be expected to be centered around such interfaces (and also around the grain boundaries). To monitor changes in the overall fraction of the low-symmetry local regions, if any, by the poling field requires a probe which is sensitive to the structure on the local scale. The measured data should also be statistically relevant in the sense of sampling the information randomly from different spatial regions (much larger than the correlation length which the technique probes) of the system. While tools such as transmission electron microscopic can give the exact nature of the local changes such as field-driven phase changes [15], the volume under examination is insignificantly small. Other local probes, for example, nuclear magnetic resonance (NMR) [16] and extended x-ray fine structure spectroscopy (EXAFS) [17], are heavily dependent on the model used for the data analysis.

A relatively less-known technique, photoluminescence (PL) of trivalent lanthanide ions, suits our purpose. The Stark lines in a PL spectrum are dependent on the local structure of the ligand environment around the lanthanide ion, making the PL signal sensitive to the local structure [18]. Further, lanthanides such as Dy^{+3}, Sm^{+3}, Eu^{+3}, Er^{+3}, Nd^{+3}, Ho^{+3}, and Tm^{+3} exhibit hypersensitive transitions, i.e., the probability of some quadrupolar transitions is greatly enhanced by increased asymmetric distribution of the ligand field around the lanthanide ion [19]. Among them, the large difference between the energy of the charge-transfer transition and the $^5D_0 \rightarrow {}^7F_2$ hypersensitive transition of Eu^{+3} makes the hypersensitive transitions in Eu^{+3} more sensitive to the local

*rajeev@iisc.ac.in

environment as compared to the hypersensitive transitions of the other trivalent lanthanide [18]. Eu^{+3} PL is therefore a nice tool for determination of local symmetry in complex structures [20,21], subtle structural changes across phase transformations induced by composition [22], temperature [23,24], pressure [25–28], and in monitoring the extent of crystallization during annealing of structural glasses [29]. It may be emphasized that unlike pressure and temperature, which are fundamental thermodynamic variables, the energy involved with electric field commonly used in experiments (few kV/cm in bulk piezoceramics) is insignificantly small to drive a system (by itself) towards a crystallographic phase transformation. However, electric field can be an influential parameter when the system is close to an interferroelectric instability and can make one ferroelectric phase grow at the expense of the other by motion of the already existing interphase boundaries and/or creation of new interphase boundaries. The change in the structural heterogeneity is therefore expected to arise primarily from the disturbances in the atomic arrangements in the proximity of the interfaces (domain walls and interphase boundaries) when the poling field acts on the system. Keeping in view the fact that the system's weak-field piezoelectric response (the d coefficients) is measured on a poled state of the specimen, understanding the influence of the poling field on the overall heterogeneity of the specimen has great significance vis-à-vis the microscopic mechanisms contributing to piezoelectricity enhancement. Our approach involves randomly dispersing Eu^{+3} ions (in dilute concentration) in the piezoelectric matrix to make them act as local structure sensors. Their distribution throughout the sample also assures that the information obtained is relevant in the statistical sense and therefore representative of the behavior of the specimen as a whole. With this as the primary motivation, we chose to use Eu^{+3} PL as the local probe, and the $BaTiO_3$-based lead-free piezoelectric $Ba(Ti_{1-x}Sn_x)O_3$ in the vicinity of the $P4mm$-$Amm2$ polymorphic phase boundary (PPB) as the piezoelectric system. $Ba(Ti_{1-x}Sn_x)O_3$ (BTS) shows high d_{33} at the $P4mm$-$Amm2$ boundary at room temperature [30,31]. We doped BTS with 0.5 mol% Eu_2O_3 to make use of the Eu^{+3} PL signal to probe the characteristics of the BTS matrix as it changes structure with composition and electric field.

II. EXPERIMENTAL

Specimens of $Ba(Ti_{1-x}Sn_x)O_3$ (BTSx) ceramics and Eu-doped $Ba(Ti_{1-x}Sn_x)O_3$:$Eu_{0.005}$ (BTSx:Eu) ceramics were prepared in close composition intervals $x = 0$, 0.02, 0.03, 0.04, 0.05, 0.06 by a conventional solid-state method [30,31]. Stoichiometric amounts of dried high-purity (Alfa Aesar) chemicals $BaCO_3$, TiO_2, SnO_2, and Eu_2O_3 were thoroughly mixed in zirconia vials and balls in acetone medium using a planetary ball mill (P5) for 10 h. Milled powders were dried and calcined at a temperature of 1120 °C for 4 h in an alumina crucible. Green pellets were made by applying uniaxial pressure in a 2% polyvinyl alcohol mixed calcined powder. Finally, sintering was done by a two-step process, first heating to 1350 °C for 4 h and then to 1550 °C for 6 h. Electrical poling was done by applying a dc electric field in the range 1–2 kV/mm for 1 h on pellet samples and then gently crushed to powder for x-ray diffraction measurements. X-ray powder-diffraction data was collected using a Rigaku Smart Lab x-ray diffractometer with Cu $K\alpha_1$ radiation in Bragg Brentano reflection geometry. Sintered pellets were ground to powder and then annealed at 500 °C for 1 h to relieve residual stress before performing x-ray diffraction measurements of unpoled samples. Photoluminescence (PL) spectroscopy data was collected from poled and unpoled powder samples using a 532-nm laser attached with LabRAM HR (HORIBA) spectrometer. A direct piezoelectric coefficient d_{33} was measured on poled pellets using a Piezotest PM300. Polarization electric-field-loop measurements were performed on Precision Premier II tester (Radiant Technologies, Inc.). Electrostrain was measured using a MTI-2300 FOTONIC sensor (MIT Instruments) attached with a Precision Premier II tester. Rietveld analysis was done using the software FULLPROF [32].

III. RESULT

A. Piezoelectric and ferroelectric characterization

Because of the strong correlation of the $P4mm$-$Amm2$ boundary with high piezoelectricity, we limited ourselves to the $Ba(Ti_{1-x}Sn_x)O_3$ compositions in the vicinity of this boundary and synthesized compositions at small concentration intervals $x = 0$, 0.02, 0.03, 0.04, 0.05, and 0.06 with 0.5 mol% Eu. From the plots shown in Fig. 1, although there

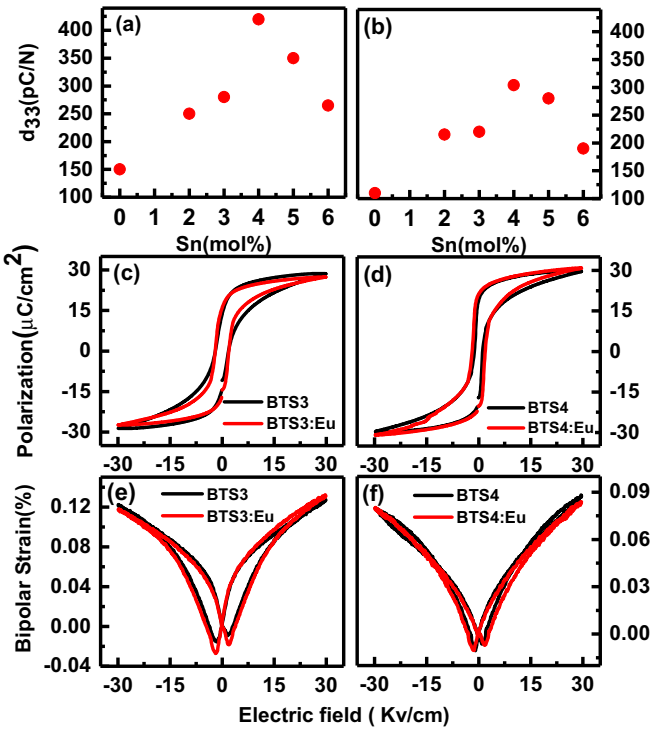

FIG. 1. (a), (b) Longitudinal piezoelectric constant (d_{33}) as a function of composition of $Ba(Ti_{1-x}Sn_x)O_3$ in Eu-free and Eu-doped specimens. (c), (d) Polarization-electric-field (P-E) hysteresis loop of undoped and doped specimens of PPB compositions $x = 0.03$ (BTS3:Eu) and $x = 0.04$ (BTS4:Eu). (e), (f) Bipolar electrostrain hysteresis of the undoped and Eu-doped PPB compositions $x = 0.03$ (BTS3:Eu) and $x = 0.04$ (BTS4:Eu).

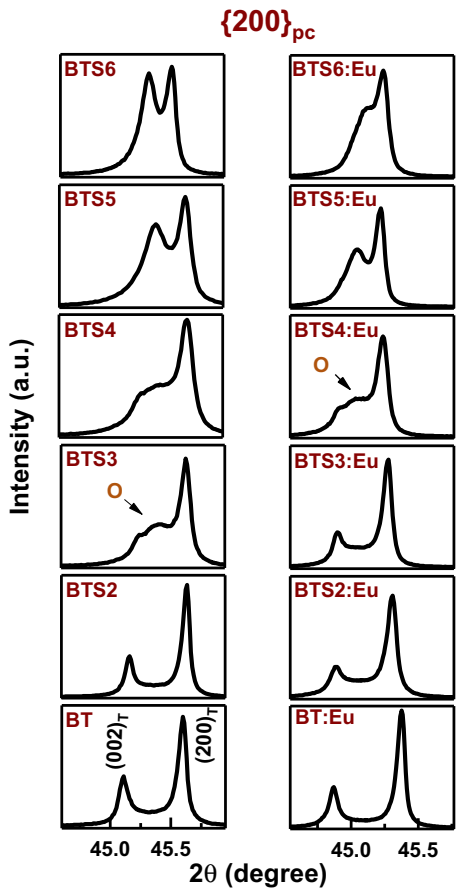

FIG. 2. Evolution of the pseudocubic $\{200\}_{pc}$ Bragg profiles of Eu-doped and undoped $Ba(Ti_{1-x}Sn_x)O_3$ ($x = 0$–0.06). The data was collected on powder specimens. The orthorhombic peak is shown by arrows.

is a slight decrease in the weak-signal piezoelectric coefficient (d_{33}) after Eu^{+3} doping, the composition dependence of the piezoelectric coefficient (d_{33}) follows the same trend for both the Eu^{+3}-doped and undoped specimens. The undoped and the Eu-doped samples exhibit almost identical polarization-field (P-E) and strain-field (S-E) hysteresis loops, suggesting that the 0.5 mol% of Eu doping does not interfere significantly with the ferroelectric behavior of the host matrix BTS. At the same time, as will be shown below, this dilute doping concentration shows a sufficiently intense PL signal for meaningful and reliable analysis.

B. Crystal structure

Figure 2 shows the x-ray powder-diffraction profiles of the pseudocubic reflection $\{200\}_{pc}$ for both Eu undoped and doped BTS. The complete x-ray diffraction (XRD) patterns are shown in Fig. S1 of the Supplemental Material [33]. The XRD pattern of $x = 0.02$ is similar to that of the parent compound $BaTiO_3$, suggesting a tetragonal ($P4mm$) structure. The higher compositions $x = 0.03$ and $x = 0.04$ show a new reflection, corresponding to the orthorhombic ($Amm2$) phase, in between the $(002)_T$ and $(200)_T$ tetragonal peaks. These compositions therefore represent the PPB. The shape of the pseudocubic $\{200\}_{pc}$ Bragg profiles of $x = 0.05$ and 0.06 is akin to what has been reported for the orthorhombic ($Amm2$) phase of the $BaTiO_3$-based piezoceramics [30,31]. The XRD Bragg profiles of the Eu-doped specimens follow the same structural evolution with composition. A slight difference is that the orthorhombic peak becomes prominently visible at $x = 0.04$ in the Eu-doped specimen, whereas in the undoped samples an orthorhombic peak can be seen even at $x = 0.03$. This indirectly confirms that the doped Eu is part of the perovskite structure, though some of them sitting on the grain boundaries cannot be ruled out. Based on its ionic radii (1.066 Å, for VIII coordination) [34], it is most likely to occupy the A site of the perovskite structure. Figure 3 shows Rietveld fitted x-ray powder-diffraction data of BTSx:E with $x = 0.00$, 0.03, 0.04, 0.06. We fitted all the diffraction data a with tetragonal $P4mm$ and orthorhombic $Amm2$ phase coexistence model. With increasing Sn concentration the increasing intensity of the orthorhombic $(440)_O$ peak in between the two tetragonal peaks $(400)_T$ and $(004)_T$ confirms the increasing fraction of the $Amm2$ phase, Fig. 3(e). Rietveld analysis of the XRD data showed that the orthorhombic phase fraction increased from 0 to 94% on increasing x from 0 to 0.06. The refined structural parameters of the tetragonal and orthorhombic phases for BTS3:Eu and BTS4:Eu are given in Tables S1 and S2 of the Supplemental Material [33].

C. Eu^{+3} photoluminescence

Figure 4 shows the Eu^{3+} PL emission spectra of the Eu-doped specimens. The spectra were collected on powder specimens of the sintered ceramics. The emission bands in the different wavelength ranges are categorized as $^5D_0 \rightarrow {}^7F_0$ (570–585 nm), $^5D_0 \rightarrow {}^7F_1$ (585–600 nm), $^5D_0 \rightarrow {}^7F_2$ (610–630 nm), $^5D_0 \rightarrow {}^7F_3$ (645–660) nm [18]. We may note that there is no noticeable emission in the same wavelength range by the host matrix (Fig. S2, Supplemental Material [33]). For the sake of consistency, we present all the PL spectra on a normalized scale. All the compositions show maximum intensity of the Stark line corresponding to the $^5D_0 \rightarrow {}^7F_1$ Stark band. The relative intensity of the $^5D_0 \rightarrow {}^7F_2$ hypersensitive Stark band increases gradually with increasing Sn content and shows maximum increase at $x = 0.04$ [as shown in the inset of Fig. 4], i.e., in the two-phase state. Interestingly, the same trend is found in the weak-field piezoelectric response (d_{33}) Fig. 1(b), suggesting a one-to-one correspondence between piezoelectric enhancement and the intensity enhancement of the $^5D_0 \rightarrow {}^7F_2$ Stark band.

We also explored the possibility of finding a correlation between the Stark lines and global structure of the ferroelectric phases by detailed examination of the different Stark bands. Figure 5(a) shows a Lorentzian fitted nonhypersensitive $^5D_0 \rightarrow {}^7F_1$ Stark band for the single-phase $P4mm$ ($x = 0$) and $Amm2$ ($x = 0.06$) compositions. A minimum of five Lorentzian profiles were required to account for all the features of this Stark band. To minimize the arbitrariness in the analysis, the number of the Lorentzian profiles was kept the same for both compositions. The details of the fitted parameters are given in Table I. For the $P4mm$ phase ($x = 0$) the characteristic Stark lines are at 594.98 and 596.78 nm. For the $Amm2$ phase ($x = 0.06$), these lines come closer, at 595.58 and 596.42 nm. We may mention that the shift, though small,

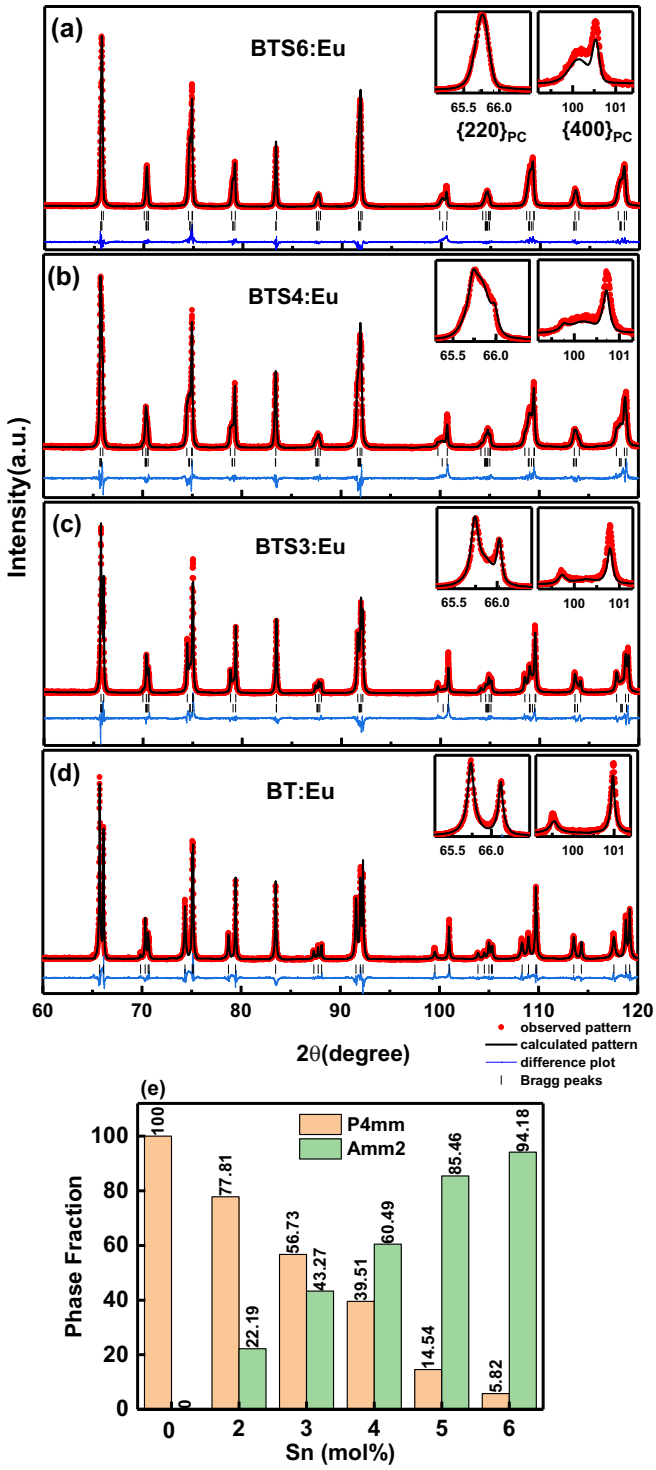

FIG. 3. Rietveld fitted x-ray (Cu $K\alpha_1$) powder-diffraction patterns of Eu-doped $BaTi_{1-x}Sn_xO_3$ for $x =$ (a) 0.06 (BTS5:Eu), (b) 0.04 (BTS4:Eu), (c) 0.03 (BTS3:Eu), and (d) 0 (BT:Eu) fitted with $P4mm$ and $Amm2$ (BT:Eu with $P4mm$ model) phase coexistence model. Insets show $\{220\}_{pc}$ and $\{400\}_{pc}$ pseudocubic Bragg profiles. (e) Phase fractions of the $P4mm$ and $Amm2$ with Sn concentration.

is outside the measurement uncertainty and was reproducible. Another notable difference, which was also reproduceable, is that the area ratio of the two signature Stark lines is 1.8 in the

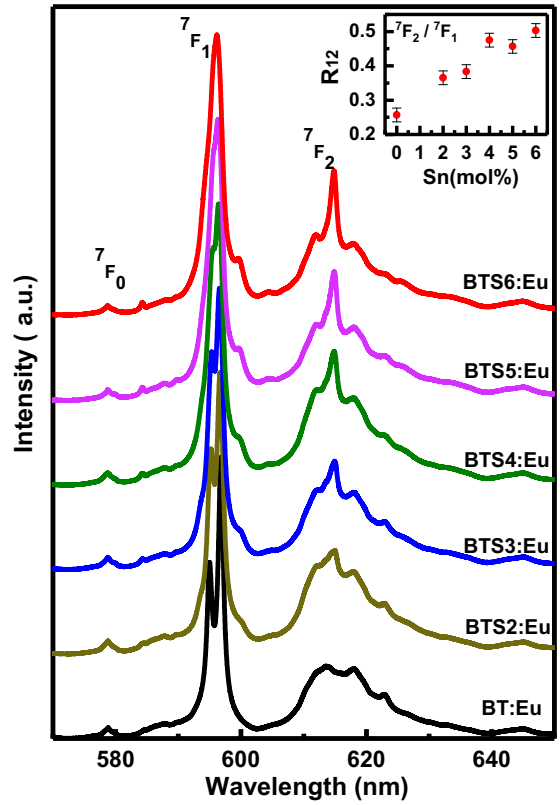

FIG. 4. Composition dependence of the Eu^{+3} PL spectrum of Eu-doped $Ba(Ti_{1-x}Sn_x)O_3$. The inset shows the composition dependence of the ratio ($R12 = {}^7F_2/{}^7F_1$) of the strongest lines in the $^7F_2$ and $^7F_1$ Stark bands.

$P4mm$ phase and 1.5 in the $Amm2$ phase. The $Amm2$ phase is also marked by the two Stark lines at 594.31 and 599.78 nm becoming relatively more intense [Fig. 5(a)]. We did a similar

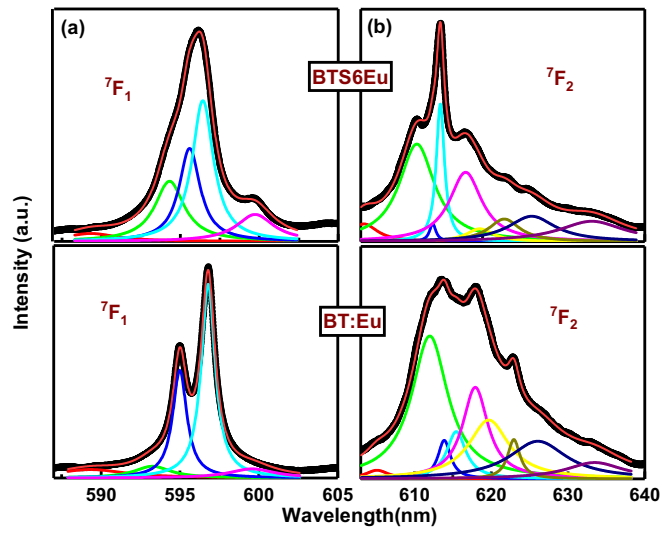

FIG. 5. (a) Lorentzian fitted nonhypersensitive Stark band $^5D_0$-$^7F_1$ in the tetragonal ($x = 0$, i.e., BT:Eu) and orthorhombic ($x = 0.06$, i.e., BTS6:Eu) compositions. (b) Lorentzian fitted hypersensitive Stark band $^5D_0 \rightarrow {}^7F_2$ of the tetragonal and orthorhombic compositions. Details of fitted parameters are given in Tables I and II.

TABLE I. Peak positions and area of Lorentzian fitted Eu^{3+} PL Stark lines corresponding to the $^5D_0 \rightarrow {}^7F_1$ Stark band in a tetragonal-dominated (BT:Eu) and orthorhombic-dominated (BTS6:Eu) host matrix.

BT:Eu		BTS6:Eu	
Peak position	Area	Peak position	Area
589.32119	0.34518	589.32171	0.23539
593.25831	0.24292	594.3106	1.01064
594.98821	0.87447	595.58225	1.11513
596.7888	1.54378	596.42136	1.70745
599.569	0.23727	599.73838	0.57184

analysis of the $^5D_0 \rightarrow {}^7F_2$, the hypersensitive Stark band, Fig. 5(b). This band required a minimum of nine Lorentzian profiles to account for all the details. The details of the fitted parameters for the $P4mm$ (BT:Eu) and the $Amm2$ (BTS6:Eu) phase are given in Table II. An important difference noted in this Stark band is the appearance of a Stark line at ∼614.8 nm in the $Amm2$ phase.

D. Eu^{+3} photoluminescence: Electric-field dependence

Figure 6 shows the Eu^{+3} PL spectra of the different compositions in their unpoled and poled states. The corresponding change in color coordinates in a Commission International de L'Eclairage (CIE) chromaticity diagram (in the limited wavelength range 570–650 nm) is also shown in Fig. 6. Since poling-induced switching of the ferroelectric-ferroelastic domains can also induce residual stress in the dense ceramic body [35], we avoided this possible influence by measuring the PL spectra on a powdered sample of the poled pellet. The powder sample is also a better representative of the bulk specimen and eliminates preferred-orientation-related effects likely to be caused by the poling field in dense ferroelectric ceramic. As has been demonstrated before [36–39], this strategy can reveal the accurate nature of the irreversible structural changes caused by the poling field, if any. As evident from Fig. 6, poling increases the intensity of the $^5D_0 \rightarrow {}^7F_2$ Stark band for all compositions, including $x = 0.00$ ($BaTiO_3$). The difference in the maximum intensity in the unpoled and the poled states for each composition is shown in Fig. 6(e). What is most remarkable is the significantly large increase (∼100% increase) in the intensity after poling of the polymorphic phase boundary compositions. As a result, the color of the emission became intense red for poled samples. Since both $x = 0.03$ and $x = 0.04$ are compositions corresponding to the $P4mm$-$Amm2$ interferroelectric boundary, we anticipated this large increase in the PL intensity of the hypersensitive band to be associated with a field-induced, irreversible $P4mm \rightarrow Amm2$ transformation. Such a transformation is easy to detect in the XRD pattern, as it would manifest as an increase in the intensity of the orthorhombic peaks with respect to the coexisting tetragonal ($P4mm$) peaks. This strategy has been used before to ascertain the poling-induced rhombohedral/monoclinic-to-tetragonal transformation in the morphotropic phase boundary (MPB) compositions of the $PbTiO_3$-$BiScO_3$ system [38,39]. Surprisingly, however, the x-ray powder-diffraction patterns before and after poling of our BTSx composition $x = 0.03$ and $x = 0.04$ (both Eu-doped and undoped) do not show significant change (Fig. 7). As demonstrated below, we reconfirmed this to be the case in the pellet specimens as well.

TABLE II. Peak positions and area of Lorentzian fitted Eu^{3+} PL Stark lines corresponding to the $^5D_0 \rightarrow {}^7F_2$ Stark band in tetragonal-dominated (BT:Eu) and orthorhombic-dominated (BTS6:Eu) host matrix.

BT:Eu		BTS6:Eu	
Peak position	Area	Peak position	Area
605.12022	0.06236	605.40884	0.24308
611.9924	1.66161	611.91295	1.91989
613.87772	0.15542	613.87078	0.06367
615.44263	0.28963	614.8112	0.62931
617.92457	0.74654	617.92652	1.24575
619.6832	0.75779	619.66875	0.19079
622.94528	0.1575	622.68559	0.38938
626.07875	0.6924	626.07125	0.66481
633.4784	0.29932	633.47303	0.73354

E. X-ray diffraction *in situ* with electric field

To ascertain if the poling field led to structural transformation or not in the PPB compositions, we carried out XRD *in situ* with the electric field on $x = 0.03$. We found that the grains near the surface of the pellets are significantly textured and broadened even in the unpoled state (Fig. S3, Supplemental Material [33]). This would make it difficult to ascertain the nature of field-induced structural changes, if any. The necessity to examine the structural changes as a function of field on specimen exhibiting no residual stress and texture forced us to adopt a different strategy wherein we performed XRD *in situ* with the electric field on unclamped free grains, i.e., powder samples. We did this by hand grinding the dense ceramic specimen to powder and annealing them to get rid of stress-induced changes, if any, incurred during the grinding process. The annealed powder was mixed with a soft polymer matrix, namely, polyvinylidene fluoride (PVDF). This strategy has the benefits of the avoiding the stress which can arise in dense ceramic specimens during field-driven domain switching due to mutual clamping of the grains [35]. The powder nature of the ceramic specimen ensures that the diffraction pattern is free of preferred orientation and residual stress before the application of the electric field. The only drawback of our approach is that the voltage applied on the polymer-ceramic composite is dropped more in the polymer region due to its relatively lower dielectric constant as compared to the ceramic. Consequently, it is not meaningful to correlate the changes in the XRD patterns with the magnitude of the total electric field applied on the polymer-ceramic composite specimen. Our interest is rather limited to determining the nature of the structural changes when the grains experience enough field for the same, irrespective of how much field we needed to apply on the composite specimen. The polymer-ceramic composites were made following the recent work of Mahale *et al.* [40]. We started with 55 vol% ceramic content to get

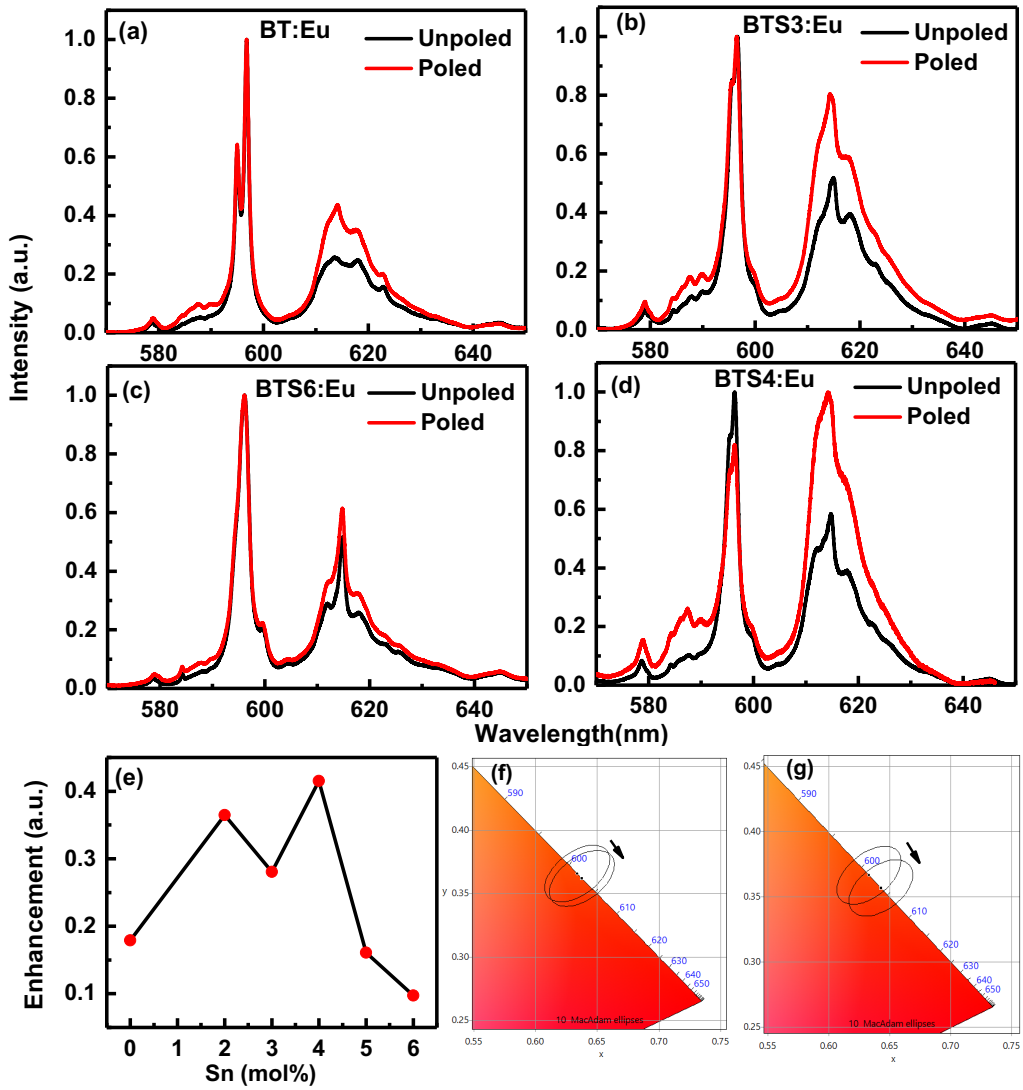

FIG. 6. PL Spectra of unpoled and poled Eu-doped (a) BT, (b) BTS3, (c) BTS6, and (d) BTS4. The corresponding change in color coordinates are displayed in the Commission International de L'Eclairage (CIE) chromaticity diagrams for PPB compositions (f) BTS3 and (g) BTS4. (e) The enhancement in the intensity of the hypersensitive band after poling for different Sn concentrations.

a homogeneous distribution of ceramic powder. The PVDF solution was prepared by dissolving 18 wt% of PVDF (Kynar-761 with Mw = 440 000 g/mol, obtained from Arkema, Inc.) in *N*, *N*-dimethylformamide (DMF) solvent. The mixture was constantly stirred on a magnetic stirrer at 60 °C for 30 min to dissolve the PVDF. The predetermined amount of BTS3Eu fine powder was then mixed with the PVDF-DMF solution, and then it was thoroughly stirred. After some time, the slurry was poured on a 50 °C heated glass substrate and dried in a hot air oven at 100 °C for 1 h to evaporate the solvent. The composite films were placed between hotplates at 170 °C and pressed with the pressure around 800 psi to remove the voids left over during the evaporation of the solvent and to make the films wrinkle free. The thickness of the films was found to be in the range of 170–250 μm.

Figure 8 shows evolution of a pseudocubic $\{200\}_{pc}$ Bragg profile with increasing electric field. With increasing electric field $(002)_T$ peak intensity increases due to switching of the 90° domain along the direction of electric field. At an applied field of 25 kV/cm the intensity of the $(002)_T$ becomes greater than that of $(200)_T$, suggesting considerable switching of the ferroelectric-ferroelastic domains. This ensures that the applied field is indeed experienced by the ceramic grains in the polymer-ceramic composite specimen. In addition to domain switching, the appearance of a new peak (marked with O in Fig. 8) in between $(200)_T$ and $(002)_T$ indicates the field-induced growth of orthorhombic phase [30,41,42]. This is more clear in the evolution of the pseudocubic $\{400\}_{pc}$ Bragg profile [Fig. 8(b)] wherein the peak corresponding to the orthorhombic phase has relatively less overlap with the $(004)_T$ and $(400)_T$ tetragonal peaks. The interesting feature is that with decreasing field, not only do the domains start reverse switching but also the intensity of the orthorhombic peak phases starts to decrease. This confirms that the electric-field-induced phase transformation is reversible to a very large extent in this system. For the sake of comparison, we also performed the *in situ* XRD experiment on the pellet. For this we focused our attention only on the $\{400\}_{pc}$ peak, as the effect

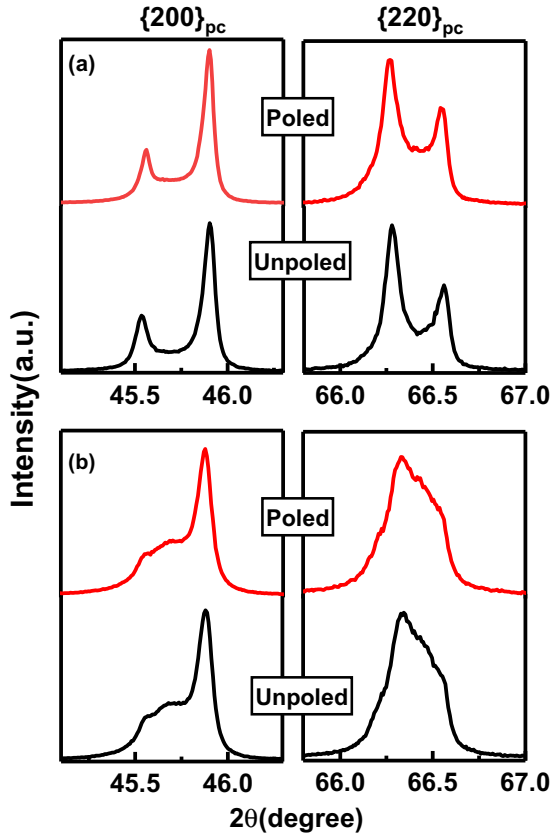

FIG. 7. Pseudocubic Bragg profiles $\{200\}_{pc}$ and $\{220\}_{pc}$ of poled and unpoled powder specimens of (a) BTS3:Eu and (b) BTS4:Eu. Bragg profiles showing the same global structure in poled and unpoled specimens.

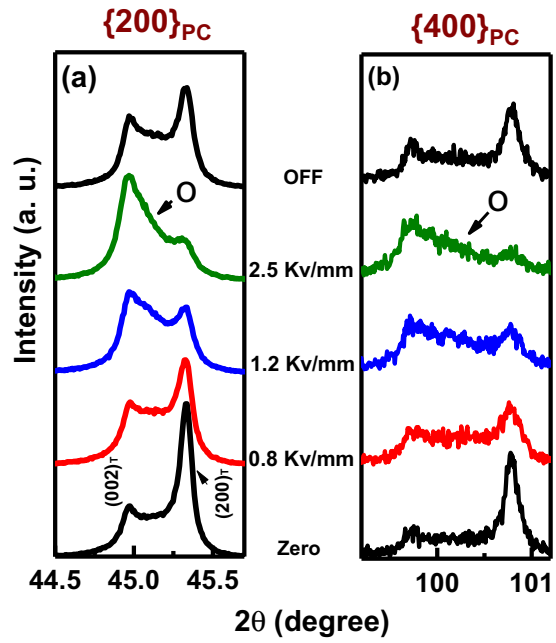

FIG. 8. Evolution of pseudocubic (a) $\{200\}_{pc}$ and (b) $\{400\}_{pc}$ Bragg profile with *in situ* electric field in BTS3Eu/PVDF composite film during increasing electric field and after the field was switched off.

of residual surface stress and preferred orientation was less for this peak as compared to the $\{200\}_{pc}$ (Fig. S3, Supplemental Material [33]). This can be understood from the fact that the grains contributing to the $\{400\}_{pc}$ profile are at more depth from the surface of the pellet. The self-texturing due to surface relaxation of domains and the corresponding residual stress is less pronounced for the grains well below the surface region since they are equally clamped from all sides. Figure 9 shows the evolution of the pseudocubic $\{400\}_{pc}$ Bragg profile with increasing and decreasing electric field. Like the free grains in the polymer-ceramic composite specimens, we do see the increase in intensity of the orthorhombic peak (marked as O in Fig. 9), confirming the field-induced $P4mm \rightarrow Amm2$ transformation in the dense ceramic specimen as well. On decreasing the field, the intensity of the orthorhombic "O" peak also decreases, thereby confirming the reverse transformation.

IV. DISCUSSION

The $^5D_0 \rightarrow {}^7F_2$ transitions of Eu^{3+} ion have been labeled "hypersensitive," which means its intensity is very much sensitive to the local symmetry around the Eu^{3+} ion. The theory of Jorgensen and Judd [19] attributes the increase in the intensity of the hypersensitive Stark band to the increased inhomogeneity in the dielectric medium surrounding the lanthanide ion. One aspect of increasing structural heterogeneity is local lowering of the symmetry, as seen by the Eu^{+3} ions embedded in the piezoelectric matrix [18]. In this context, Fan *et al.* [43] have shown that the intensity of the hypersensitive band of the Eu^{+3} PL spectrum can be tuned by varying

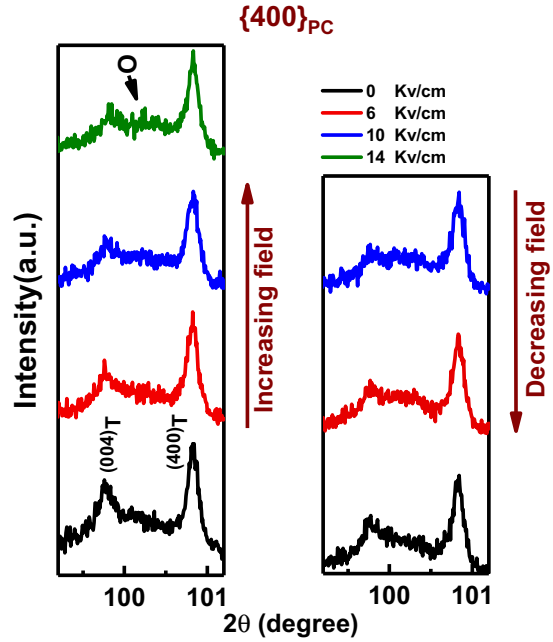

FIG. 9. Evolution of the pseudocubic x-ray $\{400\}_{pc}$ Bragg profile with electric field during increasing (left) and decreasing (right) field on a pellet specimen of BTS3:Eu.

the chemical composition of $EuCl_3$ and β-diketonate codoped gels. In the $EuCl_3$ the singly doped gel emission intensity of the nonhypersensitive $^5D_0 \rightarrow {}^7F_1$ band is stronger than the hypersensitive $^5D_0 \rightarrow {}^7F_2$ band, whereas in the $EuCl_3$ and β-diketonates the codoped gel $^5D_0 \rightarrow {}^7F_2$ intensity becomes stronger than that of the $^5D_0 \rightarrow {}^7F_1$ band. This enhancement in the intensity of the hypersensitive band is due to more Eu^{+3} ions experiencing lower symmetry in the codoped gel [39]. This aspect is more convincingly demonstrated in solid by Lourenco *et al.* [29] during crystallization of Eu-doped lead borosilicate glass. The authors showed that the intensity of the $^5D_0 \rightarrow {}^7F_2$ hypersensitive band decreases as more and more fraction of the amorphous region gets converted to the crystalline region with increasing annealing temperature. The amorphous regions being structurally disordered, the Eu^{+3} embedded in such a region would see lower symmetry than those embedded in the crystalline region. With increasing the annealing temperature, a greater fraction of the doped Eu^{+3} in the solid is in a higher-symmetry environment, thereby reducing the intensity of the $^5D_0 \rightarrow {}^7F_2$ hypersensitive band emitted by the solid. In our case, the increase in the intensity of the hypersensitive band is achieved after electric poling (Fig. 6). The enhancement is considerably large for the PPB compositions ($x = 0.03$ and $x = 0.05$) as compared to the non-PPB compositions $x = 0.00$ ($P4mm$) and $x = 0.06$ ($Amm2$). As our XRD study *in situ* with electric field suggests, the field-induced domain switching and the concomitant $P4mm \rightarrow Amm2$ is reversible to a large extent on the global length scale. At the outset this appears to contrast with the irreversible increase in the intensity of the hypersensitive band after poling. However, keeping in view that XRD pattern and the PL spectra reveals structural information on very different length scales, our results suggest a significant increase in the low-symmetry regions on the local scale after poling. These local low-symmetry regions are not of enough size to affect the global structure as seen by the XRD. From our results, it appears that although on the global scale the overall changes appear to be reversible, the entire process leaves a local residue of low-symmetry regions (monoclinic or triclinic), difficult to detect by other means. It is interesting to note that like us, Hao *et al.* have reported a significant enhancement of the hypersensitive Er^{+3} up-conversion Stark band after application of strong electric field to thin Er and Yb codoped $BaTiO_3$ epitaxial film on (001)-oriented $SrTiO_3$ substrate [44]. Yb was used as a sensitizer to increase the pumping efficiency as it enhances the energy transfer from Yb^{+3} to Er^{+3} ions when the system is pumped by infrared light. The intensity of the up-conversion green hypersensitive band increased by 2.7 times when an electric field of 125 kV/cm was applied to the film. Although no field-induced structural study was reported, we anticipate the same mechanism to be operative for the intensity enhancement of the Er^{+3} hypersensitive band. As shown in Fig. 6, to some extent our Eu-doped $BaTiO_3$ also shows some increase in the intensity of the Eu^{+3} hypersensitive Stark band. Although, unlike the PPB compositions ($x = 0.03$ and 0.04), pure BT does not explicitly show field-induced $P4mm \rightarrow Amm2$ transformation on the global scale, short-ranged monoclinic order has been reported during the $P4mm$-$Amm2$ transformation in $BaTiO_3$ [45–48]. The possibility of the monoclinic phase in $BaTiO_3$ is also known by first-principles and phenomenological calculations [48,49]. In view of this, although we have fitted our diffraction data with tetragonal and orthorhombic phase coexistence models, the presence of local monoclinic distortions cannot be ruled out [30,47]. In contrast to bulk ceramics and single crystals, the crystal structure of epitaxial $BaTiO_3$ films can be more susceptible to field-induced structural changes as the biaxial stress at the film-substrate interface can significantly change the nature of the structural stability [50].

In another related work, Sun *et al.* [51] reported PL emission of Pr^{+3} ions doped in $0.5Ba_{0.7}Ca_{0.3}TiO_3$-$0.5Ba(Ti_{0.8}Zr_{0.2})O_3$ (BCTZ) polycrystalline piezoceramic. This composition is well known for its extraordinary high piezoelectricity ($d_{33} \sim 600$ pC/N) [3]. The structural state of MPB composition of BCTZ has been in controversy with the first report suggesting the coexistence of tetragonal ($P4mm$) and rhombohedral ($R3m$) phases [3]. Later studies identified a narrow orthorhombic ($Amm2$) region in the phase diagram of the BCTZ system and associated the large piezoelectricity to the $P4mm$-$Amm2$ phase boundary [4]. Sun *et al.* [51] showed that the intensity of the red emission line of Pr^{+3} at 650 nm decreases significantly on the first application of strong field and related this to increased symmetry ($R3m$) of the phase transformed by the electric field. In the corresponding structural work, the authors showed that after sufficient poling, the $\{200\}_{pc}$ Bragg profile appears as a singlet and interpreted this to imply a transformation of the system to the rhombohedral phase. This interpretation cannot be treated as conclusive, since the orthorhombic and the rhombohedral peaks are known to occur at almost similar 2θ positions in BCTZ [42]. The residual stress and preferred orientation of the poled specimen can lead to considerable broadening of the Bragg profiles and alters the relative intensity of the Bragg peaks, making accurate structural analysis difficult. By circumventing these problems using a "powder poling technique" Brajesh *et al.* have demonstrated that poling rather increases the fraction of the orthorhombic phase in this system [42]. This contrasts with the viewpoint of Sun *et al.* [51], who suggested a field-induced $P4mm \rightarrow R3m$ transformation to rationalize the decrease in the intensity of the red emission line of Pr^{+3} at 650 nm. Since this line is not part of the hypersensitive band of Pr^{+3}, the decrease in the intensity need not necessarily be related to symmetry change. In view of this, it is worthwhile to revisit the structure-PL correlation in the BCTZ system.

V. CONCLUSIONS

In summary, we show that the $^5D_0 \rightarrow {}^7F_2$ hypersensitive Stark band in the Eu^{+3} photoluminescence spectra can be used as a probe to examine local structural heterogeneity in piezoelectrics. We exploit this feature to examine how the mandatory treatment of poling a piezoceramic to make it piezoactive influences the overall structural heterogeneity of the lead-free piezoelectric system $Ba(Ti_{1-x}Sn_x)O_3$ as it passes through the tetragonal ($P4mm$)- orthorhombic ($Amm2$) phase boundary. We found that despite the large reversibility of the

poling-induced $P4mm$-$Amm2$ transformation on the global scale, the polymorphic phase boundary (PPB) compositions shows ∼100% irreversible increase in the intensity of the hypersensitive Stark band in the PPB compositions. This correlates very well with the trend in the piezoelectric response. Our study shows that the role of poling a piezoelectric specimen is not merely limited to making the ceramic piezoactive by aligning the domains along the field direction, but it also plays a synergistic role in enhancing the performance of the MPB/PPB piezoceramic by increasing the overall structural-polar heterogeneity. We hope that this insight will provide a guideline for systematic design of high-performance piezoelectric materials, keeping the structural heterogeneity aspect as an important consideration.

ACKNOWLEDGMENT

R.R. acknowledges the Science and Engineering Research Board, Department of Science and Technology, Government of India, for financial assistance (Grant No. EMR/2016/001457).

[1] European Commission, Directive 2002/95/EC of the European Parliament and of the Council of 27 Jan 2003 on the restriction of the use of certain hazardous substances in electrical and electronic equipment, Off. J. Eur. Union **L37**, 19 (2003).
[2] European Commission, Directive 2011/65/EC of the European Parliament and of the Council of 27 Jan 2003 on the restriction of the use of certain hazardous substances in electrical and electronic equipment, Off. J. Eur. Union **L174**, 88 (2011).
[3] W. Liu and X. Ren, Phys. Rev. Lett. **103**, 257602 (2009).
[4] D. S. Keeble, F. Benabdallah, P. A. Thomas, M. Maglione, and J. Kreisel, Appl. Phys. Lett. **102**, 092903 (2013).
[5] H. Fu and R.E. Cohen, Nature (London) **403**, 281 (2000).
[6] D. Damjanovic, J. Am. Ceram. Soc. **88**, 2663 (2005).
[7] D. Damjanovic, Rep. Prog. Phys. **61**, 1267 (1998).
[8] S. Trolier-McKinstry, N. B. Gharb, and D. Damjanovic, Appl. Phys. Lett. **88**, 202901 (2006).
[9] Y. M. Jin, Y. U. Wang, A. G. Khachaturyan, J. F. Li, and D. Viehland, Phys. Rev. Lett. **91**, 197601 (2003).
[10] S.-E. Park, S. Wada, L. E. Cross, and T. R. Shrout, J. Appl. Phys. **86**, 2746 (1999).
[11] S. Wada, S. Suzuki, T. Noma, T. Suzuki, M. Osada, M. Kakihana, S.-E. Park, L. E. Cross, and T. R. Shrout, Jpn. J. Appl. Phys. **38**, 5505 (1999).
[12] Y. Nahas, A. Akbarzadeh, S. Prokhorenko, S. Prosandeev, R. Walter, I. Kornev, J. Iniguez, and L. Bellaiche, Nat. Commun. **8**, 15944 (2017).
[13] F. Li, D. Lin, Z. Chen, Z. Cheng, J. Wang, C. Li, Z. Xu, Q. Huang, Z. Liu, L. Q. Chen, T. R. Shrout, and S. J. Zhang, Nat. Mater. **17**, 349 (2018).
[14] B. Narayan, J. S. Malhotra, R. Pandey, K. Yaddanapudi, P. Nukala, B. Dkhil, A. Senyshyn, and R. Ranjan, Nat. Mater. **17**, 427 (2018).
[15] C. Ma, H. Guo, S. P. Beckman, and X. Tan, Phys. Rev. Lett. **109**, 107602 (2012).
[16] P. B. Groszewicz, H. Breitzke, R. Dittmer, E. Sapper, W. Jo, G. Buntkowsky, and J. Rödel, Phys. Rev. B **90**, 220104(R) (2014).
[17] B. N. Rao, L. Olivi, V. Sathe, and R. Ranjan, Phys. Rev. B **93**, 024106 (2016).
[18] K. Binnemans, Coord. Chem. Rev. **295**, 1 (2015).
[19] C. K. Jorgensen and B. R. Judd, Mol. Phys. **8**, 281 (1964).
[20] A. Seminara and A. Musumeci, Inorg. Chem. Acta. **95**, 291 (1984).
[21] D. A. Durham, G. H. Frost, and F. A. Hart, J. Inorg. Nucl. Chem. **31**, 833 (1969).
[22] D. T. Tu, Y. S. Liu, H. M. Zhu, R. F. Li, L. Q. Liu, and X. Y. Chen, Angew. Chem. Int. Ed. **52**, 1128 (2013).
[23] E. Moret, F. Nicolo, J. -C. G. Bunzli, and G. Chapius, J. Less Common Met. **171**, 273 (1991).
[24] L. I. Pesterfield, N. A. Coker, and N. A. Stump, Spectrosc. Lett. **33**, 585 (2000).
[25] M. Maczka, W. Paraguassu, A. G. Souza Filho, P. T. C. Freire, J. Mendes Filho, and J. Hanuza, Phys. Rev. B **77**, 094137 (2008).
[26] G. Chen, R. G. Haire, J. R. Petereson, and M. M. Abraham, J. Phys. Chem. Solids **55**, 313 (1994).
[27] D. Machon, V. P. Dmitriev, V. V. Sinitsyn, and G. Lucazeau, Phys. Rev. B **70**, 094117 (2004).
[28] V. Lavin, T. Troster, U. R. Rodriguez-Mendoza, I. R. Martin, and V. D. Rodriguez, High Pressure Res. **22**, 111 (2002).
[29] S. A. Lourenco, N. O. Dantas, E. O. Serqueira, W. E. F. Ayta, A. A. Andrade, M. C. Filadelpho, J. A. Sampaio, M. J. V. Bell, and M. A. Pereira-da-Silva, J. Lumin. **131**, 850 (2011).
[30] A. K. Kalyani, H. Krishnan, A. Sen, A. Senyshyn, and R. Ranjan, Phys. Rev. B **91**, 024101 (2015).
[31] A. K. Kalyani, K. Brajesh, A. Senyshyn, and R. Ranjan, Appl. Phys. Lett. **104**, 252906 (2014).
[32] J. Rodrigues-Carvajal, FullPROF, A Rietveld Refinement and Pattern Matching Analysis Program (Laboratories Leon Brillouin [CEA-CNRS], France, 2000).
[33] See Supplemental Material at http://link.aps.org/supplemental/10.1103/PhysRevB.98.094111 for experimental details.
[34] R. D. Shannon, Acta Cryst. A **32**, 751 (1976).
[35] D. A. Hall, A. Steuwer, B. Cherdhirunkorn, T. Mori, and P. J. Withers, Acta Mater. **54**, 3075 (2006).
[36] B. N. Rao and R. Ranjan, Phys. Rev. B **86**, 134103 (2012).
[37] B. N. Rao, R. Datta, S. S. Chandrashekaran, D. K. Mishra, V. Sathe, A. Senyshyn, and R. Ranjan, Phys. Rev. B **88**, 224103 (2013).
[38] K. V. Lalitha, A. N. Fitch, and R. Ranjan, Phys. Rev. B **87**, 064106 (2013).
[39] D. K. Khatua, K. V. Lalitha, C. M. Fancher, J. L. Jones, and R. Ranjan, Phys. Rev. B **93**, 104103 (2016).
[40] B. Mahale, R. Pandey, N. Kumar, and R. Ranjana, J. Appl. Phys. **122**, 154105 (2017).
[41] K. Brajesh, K. Tanwar, M. Abebe, and R. Ranjan, Phys. Rev. B **92**, 224112 (2015).
[42] K. Brajesh, M. Abebe, and R. Ranjan, Phys. Rev. B **94**, 104108 (2016).

[43] X. Fan, X. Wu, M. Wang, J. Qiu, and Y. Kawamoto, Mater. Lett. **58**, 2217 (2004).
[44] J. Hao, Y. Zhang, and X. Wei, Angew. Chem. **50**, 6876 (2011).
[45] Ch. Eisenschmidt, H. T. Langhammer, R. Steinhausen, and G. Schmidt, Ferroelectrics **432**, 103 (2012).
[46] A. K. Kalyani, D. K. Khatua, B. Loukya, R. Datta, A. N. Fitch, A. Senyshyn, and R. Ranjan, Phys. Rev. B **91**, 104104 (2015).
[47] T. T. A. Lumen, Y. Gu, J. Wang, S. Lei, F. Xue, A. Kumar, A. T. Barnes, E. Barnes, S. Denev, A. Belianinov, M. Holt, A. N. Morozovska, S. V. Kalinin, L-Q. Chen, and V. Gopalan, Nat. Commun. **5**, 3172 (2014).
[48] L. Bellaiche, A. Garcia, and D. Vanderbilt, Phys. Rev. B **64**, 060103(R) (2001).
[49] D. Vanderbilt and M. H. Cohen, Phys. Rev. B **63**, 094108 (2001).
[50] O. Diéguez, S. Tinte, A. Antons, C. Bungaro, J. B. Neaton, K. M. Rabe, and D. Vanderbilt, Phys. Rev. B **69**, 212101 (2004).
[51] H. L. Sun, X. Wu, T. H. Chung, and K. W. Kwok, Sci. Rep. **6**, 28677 (2016).